**Supporting Information**

# Efficient three-phase electrocatalytic $CO_2$ reduction to formate on superhydrophobic Bi-C interfaces

Yifan Jiang,[a] Xiaodong Zhang,[b] Dafu Xu,[a] Wenzhang Li,[a] Min Liu,[b] Xiaoqing Qiu*[a]

**Experimental Procedures**

**Computational details.**

The spin-polarized DFT calculations were performed using Vienna Ab initio simulation package (VASP), and we exchanged the plane-wave basis sets and correlational functional in Perdew−Burke−Ernzerhof (PBE). The bulk Bi structure was optimized, and the result of lattice parameters is that a = 4.809 Å and α = 57.03°. To establish slab models, the optimized bulk Bi structure was cleaved with the surface orientation of (012) and (110). Then, the bottom layer was fixed and a vacuum layer ~20 Å was additionally included to avoid the interaction of artificial interslab. 9 × 9 × 9 mesh was applied to optimize original Bi bulk structure, 2 × 3 × 1 mesh for (110) slab model and 2 × 2 × 1 mesh for Bi (012) slab models. The kinetic energy cutoff was as 500 eV, and the projector augmented wave (PAW) method was used for the description of the core electrons. We diagonalized the partial Hessian matrix including the vibrational entropy and enthalpy to the DFT self-consistent-field (SCF) energy to compute the binding free energies (ΔGB) of possible intermediate states of H, OCOH, and HCOOH.

**Material Synthesis and Characterization.**

Chemical reagent. 1,3,5-benzenetricarboxylic acid ($H_3BTC$), hydrochloric acid (HCl), bismuth nitrate pentahydrate ($Bi(NO_3)_3{\cdot}5H_2O$) and methanol anhydrous were purchased from Shanghai Aladdin and used without further purification. Nafion 117 membrane and Nafion (5 wt%) were purchased from Dupon. The carbon paper was

purchased from TORAY. The H-cell, platinum electrode and platinum Electrode holder were purchased from Tianjin Aida Hengsheng Technology Co. LTD. The Ag/AgCl electrode was purchased from Wuhan Clairvoyant Technology Co. LTD. High purity carbon dioxide gas (99.999%) was purchased from Changsha Mande Gas Co. LTD.

**Preparation of Bi-MOF.**

The synthesis was carried out under solvothermal conditions in 100 mL Teflon lined steel reactor. $H_3BTC$ (750 mg) and $Bi(NO_3)_3{\cdot}5H_2O$ (230 mg) were dissolved with 60 mL of MeOH at room temperature, and then stirred for 10 min to form a transparent solution. The solution transferred to a 100 mL Teflon-lined stainless steel autoclave, which was sealed and allowed to react at 393 K for 24 h. The obtained white powder were collected by filtration, and washed with MeOH, and dried in an oven (333 K, 4 h).

**Synthesis of Bi-C.**

The as-prepared Bi-MOF precursor was placed in a porcelain boat and and heated in the tube furnace (OTF-1200X Hefei Kejing Material Technology Co. LTD) to 473 K for 2 h, and then heated to 663, 723, 923 and 1123 K, respectively for 2.5 h to get Bi-C/663, Bi-C/723, Bi-C/923 and Bi/C/1123 (heating rate 2 K /min).

**Preparation of bulk Bi.**

The bulk Bi was prepared by electrodeposition method. Aqueous solution was obtained by mixing 0.97 g $Bi(NO_3)_3{\cdot}5H_2O$ , 4 ml HCl and 60 mL $H_2O$. The bulk Bi was

carried out by galvanostatic deposition in a standard three electrode system with a working electrode of Cu metal film, an Ag/AgCl reference electrode and a platinum counter electrode at 4.8 mA $cm^{-2}$ for 380s.

**Materials characterization.**

The crystalline structures and phase of the materials were explored using power X-ray diffraction measurement technique (XRD) with a Cu Ka radiation (AXS D8 Advance, Germany).The XPS analyse was performed on Thermo ESCALAB (250XI, USA). The SEM was carried out by MIRA3 TESCAN. FT-IR spectra were recorded on a FT-IR spectrometer (Vertex V80, Germany). TGA was performed in Ar atmosphere (Netzsch, Germany). TEM images were obtained to observe the microstructures of Bi-C (Jeol 2100F, Japan). 1H NMR was recorded with a Bruker Advance 400. The Raman was carried out by LabRam HR Evolution.The XANES spectra were measured at National Synchrotron Radiation Laboratory, University of Science and Technology of China. The contact angle was measured by contact-angle system (Biolin Scientific, Finland).

**Electrochemical Measurements.**

The H-type cell was used as the electrolyzer for $CO_2$ electrochemical reduction with 0.5 M $KHCO_3$ (pH=7). Nafion-117 membrane was inserted between the cathodic and anodic chamber. A mass flow controller was used to set the $CO_2$ flow rate at 20 sccm. LSV and i-t curves were collected using CHI 660E potentiostat. The EIS curves was measured in a frequency range from 10000 to 0.01 Hz at potential of 1.4 V vs.Ag/AgCl using Princeton Versa STAT 3F. The measured potential (Ag/AgCl) could

be converted to the reversible hydrogen electrode (RHE) using the Nernst function: $V_{RHE}= V_{Ag/AgCl} + 0.222 + 0.0592 \times pH$.[1] We conducted chronopotentiometry experiments at a large range of -0.86 to -1.26V vs. RHE, which were performed at each potential for 30 min. The value of the current density is relatively stable for 30 min and only fluctuate in a small range, and we chose the accurate value of the current density. More than two independent runs we collected, and we collected 1800 date points for each run. The detail i-t curves are showed in Fig. S10, Fig. S12 and Fig. S15. The resulting gaseous products were periodically sampled every 12 min and detected by gas chromatography (GC), while the liquid products were examined using nuclear magnetic resonance (NMR) spectroscopy at the end of each chronopotentiometry experiments process (Fig S11). The faraday efficiency of gas products was calculated by the equation (the value of the molar volume of the gas is 24.48 in 298.15 K):

$$FE = \frac{c(ppm) \times 10^{-6} \times 1mL \times 10^{-3} \times 96485(C/mol) \times 2 \times 27 \times 0.74}{24.48(L/mol) \times 10^{-3} \times I \times 60}$$

The peak in NMR at 8.39 indicate the H in $HCOO^-$, and the n($HCOO^-$) could be calculated by the relationship between the n(HCOOH) and peak area from NMR (Figure S11).

The FE of HCOOH can be calculated by the equation:

$$FE = \frac{n(HCOOH)(mol) \times 96485(C/mol) \times 2}{Transfer\ charge}$$

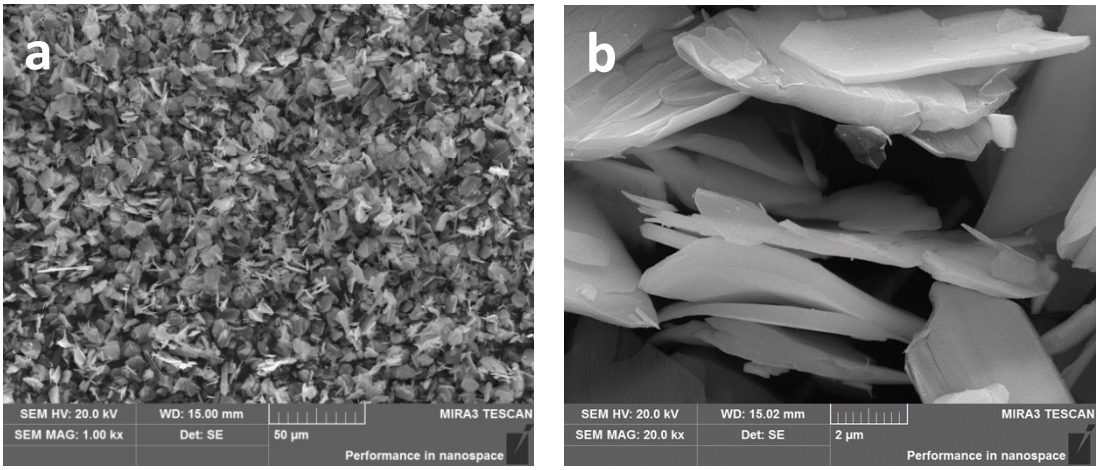


**Fig. S1** (a,b) SEM image of Bi-MOF with different magnifications.

The Bi-MOF precursor synthesized by solvothermal method exhibits nanosheet-like morphology with the average thickness of nanosheets of 100-200nm.

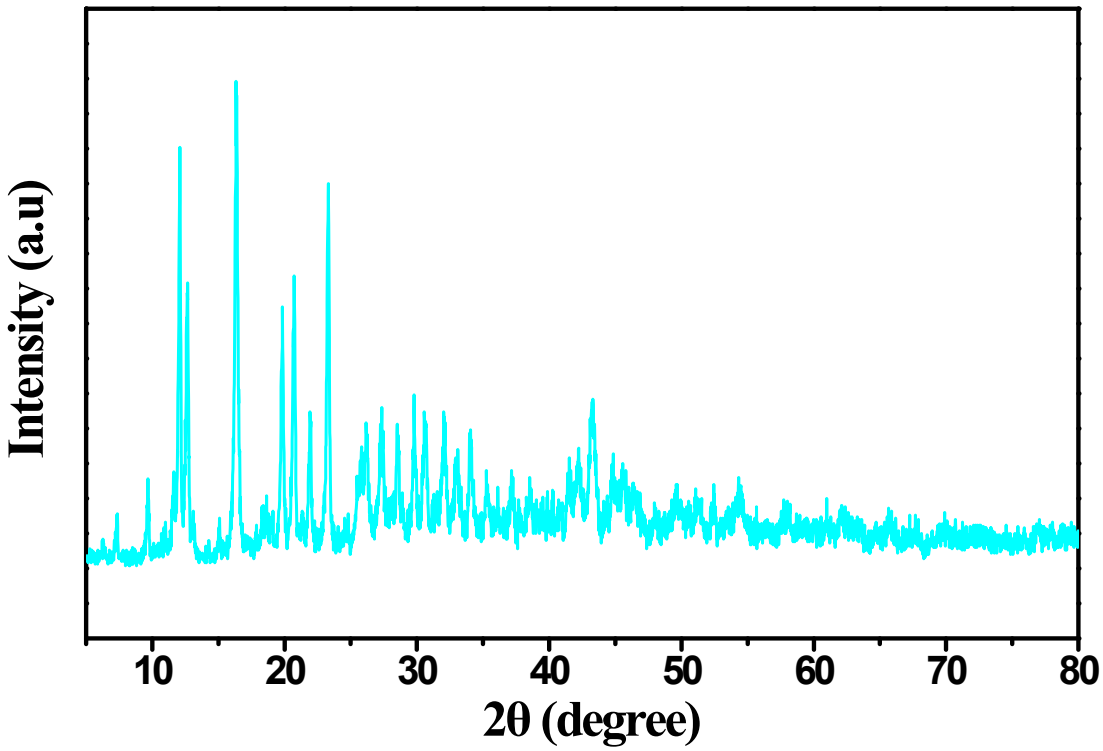


**Fig. S2** XRD pattern of prepared Bi-MOF.

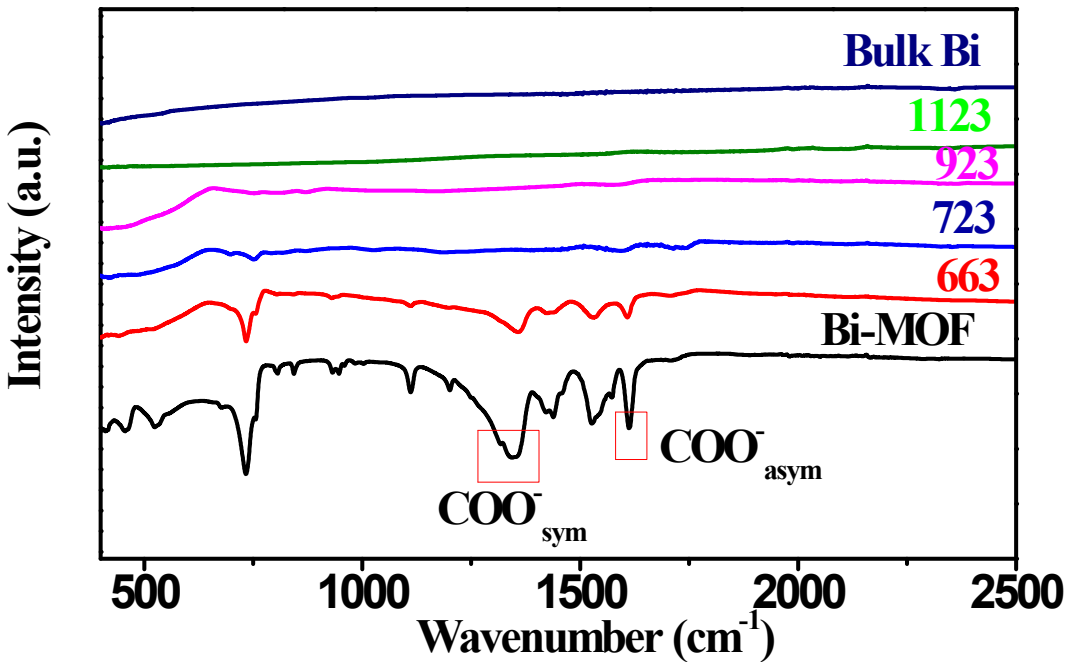


**Fig. S3** The IR spectra of the Bi-MOF, Bi-C catalysts obtained from various temperature, and Bulk Bi.

Two obvious strong peaks at 1616 $cm^{-1}$ and 1350 $cm^{-1}$ are observed for Bi-MOF, which are assigned to the asymmetric and symmetric vibrations of carboxylate anionsin BTC anions, respectively.[2] The shift of the two peaks (1616 $cm^{-1}$ and 1350 $cm^{-1}$ ) to shorter wavenumber compared with $H_3BTC$ ( 1720 $cm^{-1}$ and 1403 $cm^{-1}$ ),[3] suggesting the coordination of the $OCOO^-$ anions with bismuth. The peak at 525 $cm^{-1}$ related to the symmetrical stretching vibration of the Bi-O bond further supports the bonding of Bi cation and BTC anions.[4]

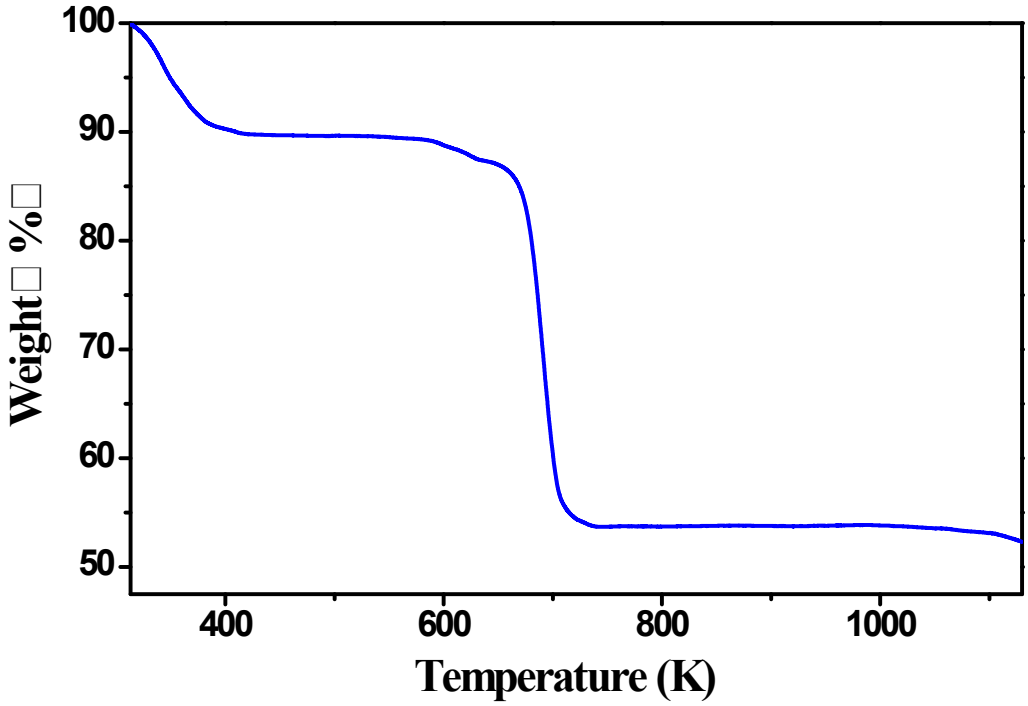


**Fig. S4** TGA curve of Bi-MOF in Ar.

When the temperature was increased to be 480 K, the rapid weight loss was about 10 wt%, corresponding to the loss of adsorbed $H_2O$ molecules. When the temperature was further increased to 650 K, about 4 wt% weight loss was observed, corresponding to the removal of coordinated $H_2O$ molecule.[5] The weight loss reaches 47 wt%, implying a greater extent of decomposition of Bi-MOF.

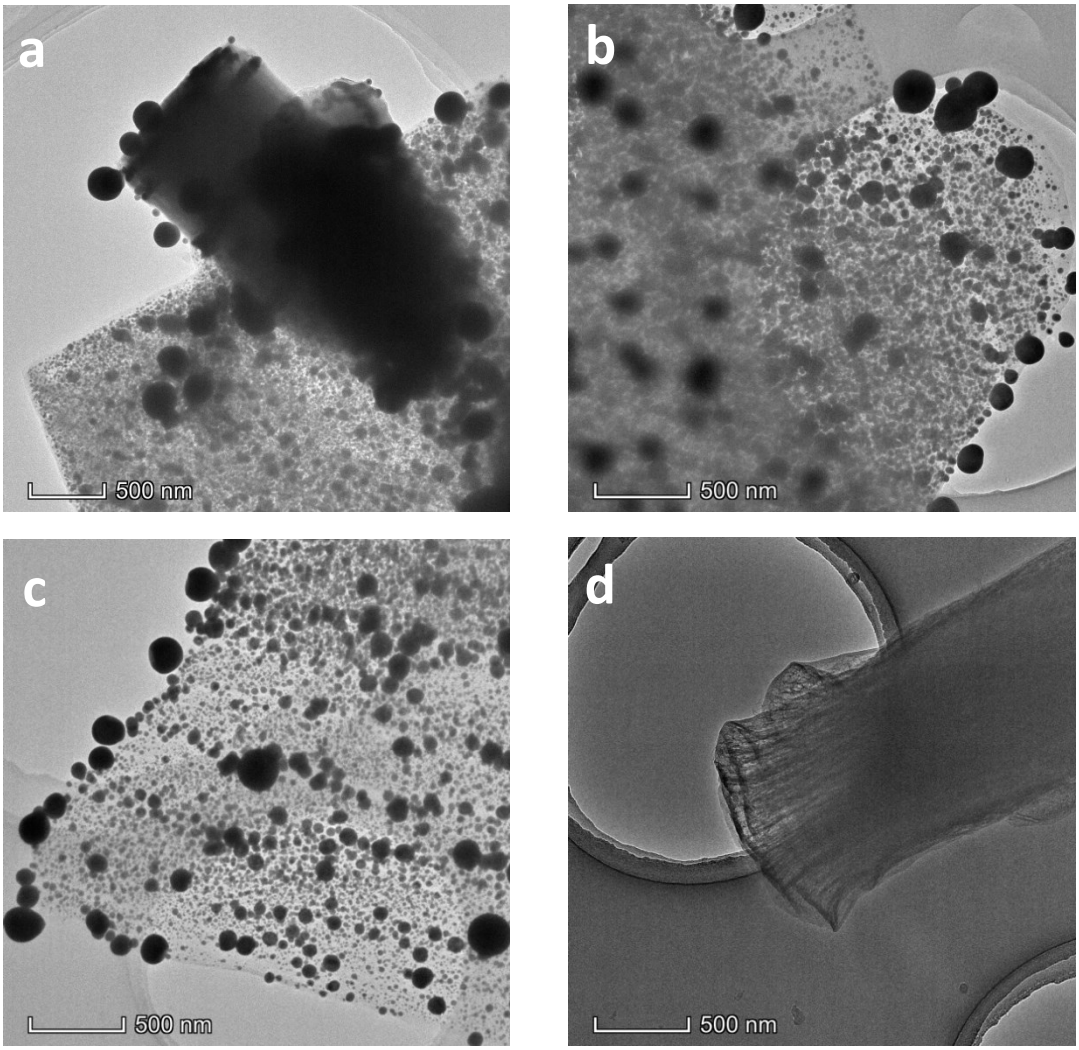


**Fig. S5** TEM images of a) Bi-C/663, b) Bi-C/723, c) Bi-C/923, and d) Bi-C/1123.

During the carbonization process of Bi-MOFs, the metallic Bi was formed under the strong reduction atmosphere, and should exist as liquid state. As the pyrolysis temperature increasing, some parts of the liquid Bi vaporized and flew away with Ar stream. When the tube furnace was cooled naturally, the liquid Bi recrystallized into the pearl-like solid nanoparticles on the carbon nanosheets. Interestingly, once the pyrolysis temperature reached 1123 K, the most amount of Bi vanished, which provides a good opportunity to observe the microstructure of the carbon substrates.

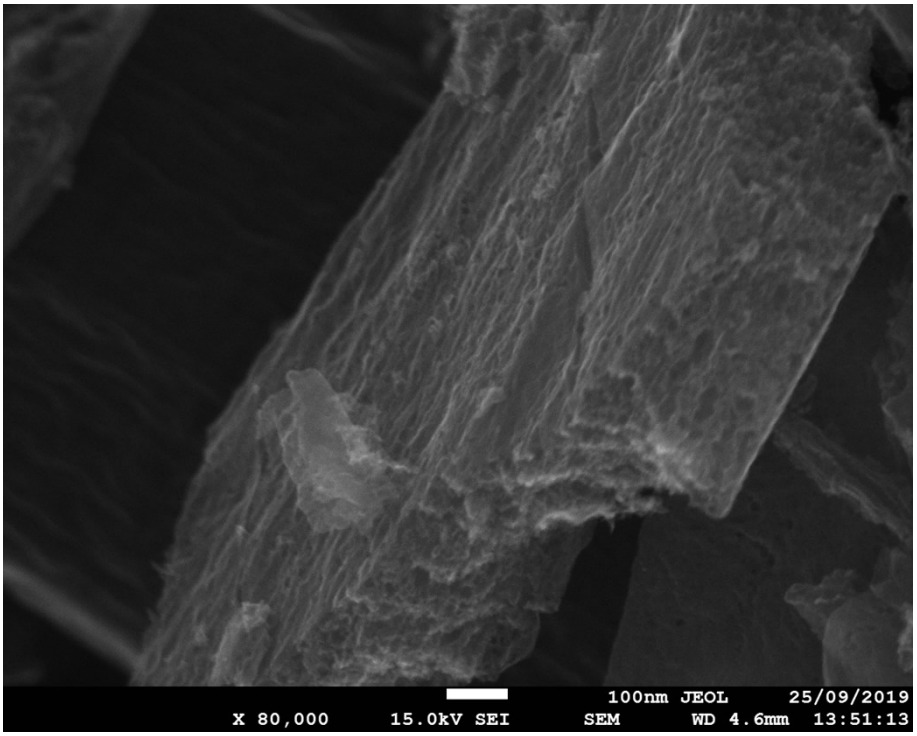


**Fig. S6** SEM image of Bi-C/1123.

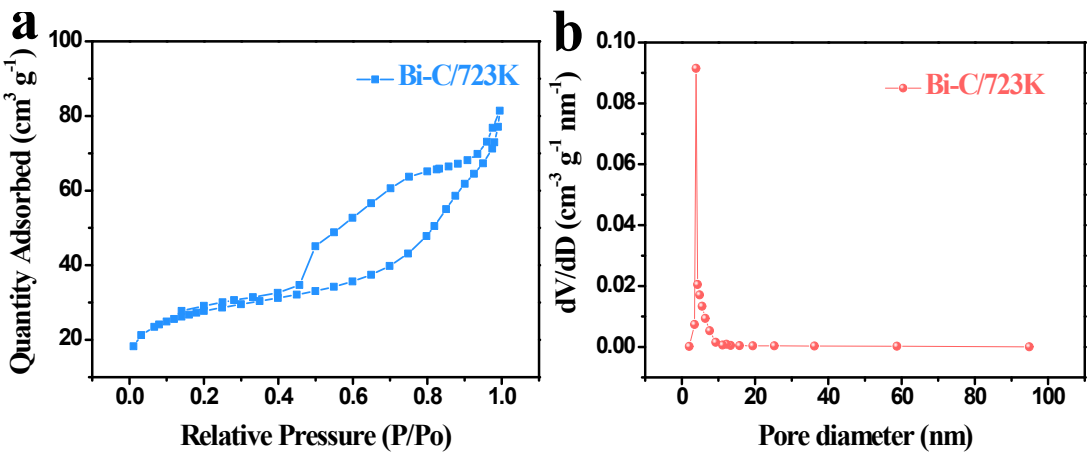


**Fig. S7** a) Nitrogen sorption isotherms, and b) Pore size distribution of Bi-C/723K.

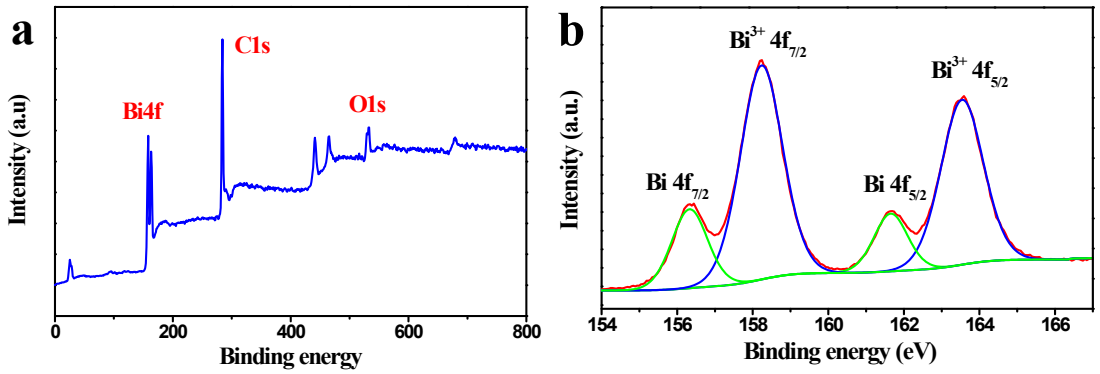


**Fig. S8** XPS signals of a) Bi-C, b) 4f of $Bi^0$ and $Bi^{3+}$.

The full-scale XPS spectrum shows three obvious peaks of Bi, C and O (Fig. S8a). As shown in Fig. S8b, the Bi 4f core-level XPS spectrum shows two sets of photoelectron signals. The peaks at 156.3 and 161.6 eV correspond to metallic $Bi^0$ 4f7/2 and 4f5/2, which coincides with the XAFS results. However, while the other two peaks at 158.2 and 163.5 eV are attributed to $Bi^{3+}$ 4f7/2 and 4f5/2, indicating that the surface of the metallic Bi nanoparticles was oxidized by exposure to ambient atmosphere. Such thin skin of $Bi_2O_3$ can be reduced to metallic during the ECR process, when the applied potential is over -0.9V vs. RHE[6].

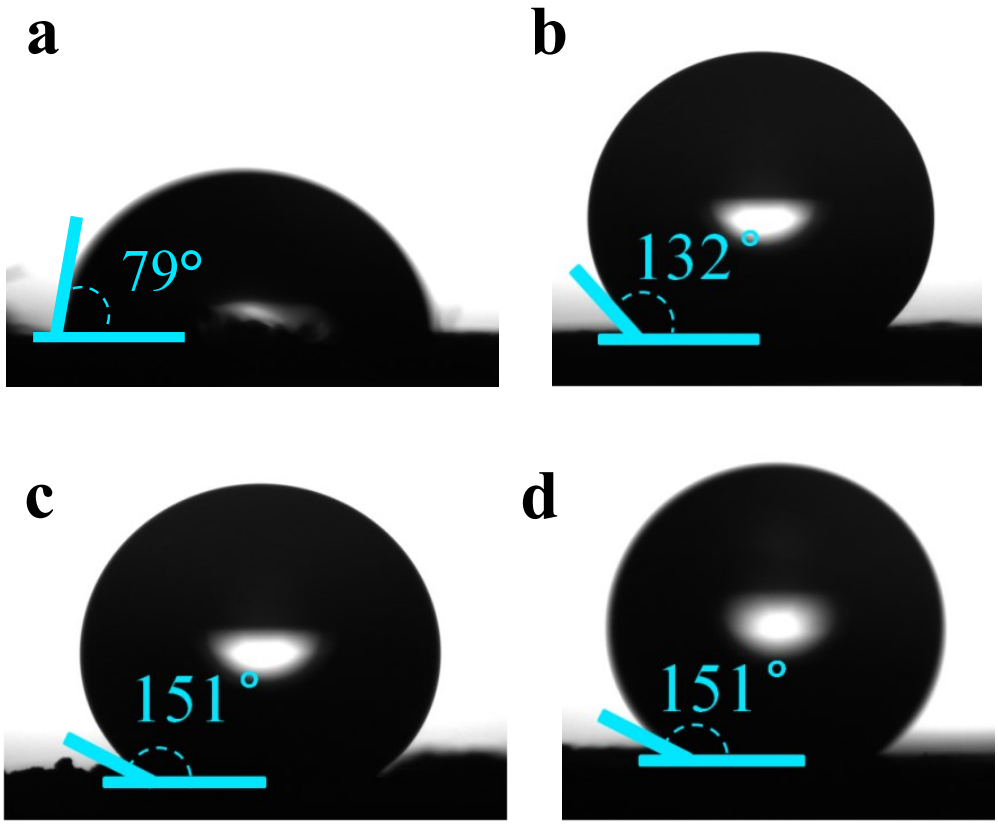


**Fig. S9** The water droplets photographs of the a) bulk Bi, b) Bi-C/663, c) Bi-C/923 and d) Bi-C/1123.

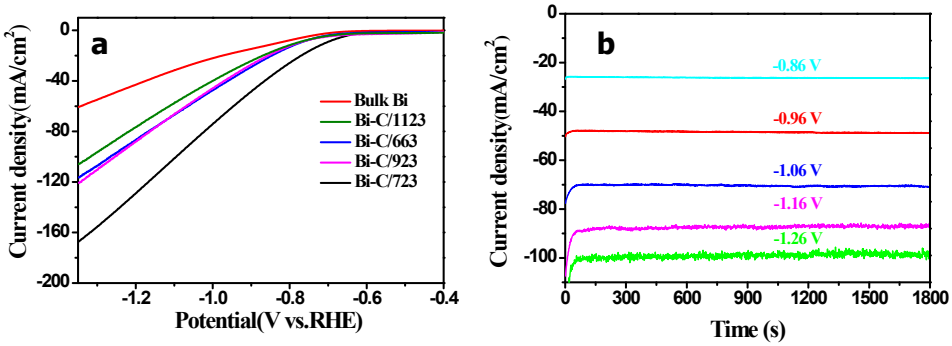


**Fig. S10 a)** The linear sweep voltammetric (LSV) curves of Bi-C materials in $CO_2$-saturated 0.5 M $KHCO_3$. b) The amperometric i-t Curves for the detailed ECR process of Bi-C/723.

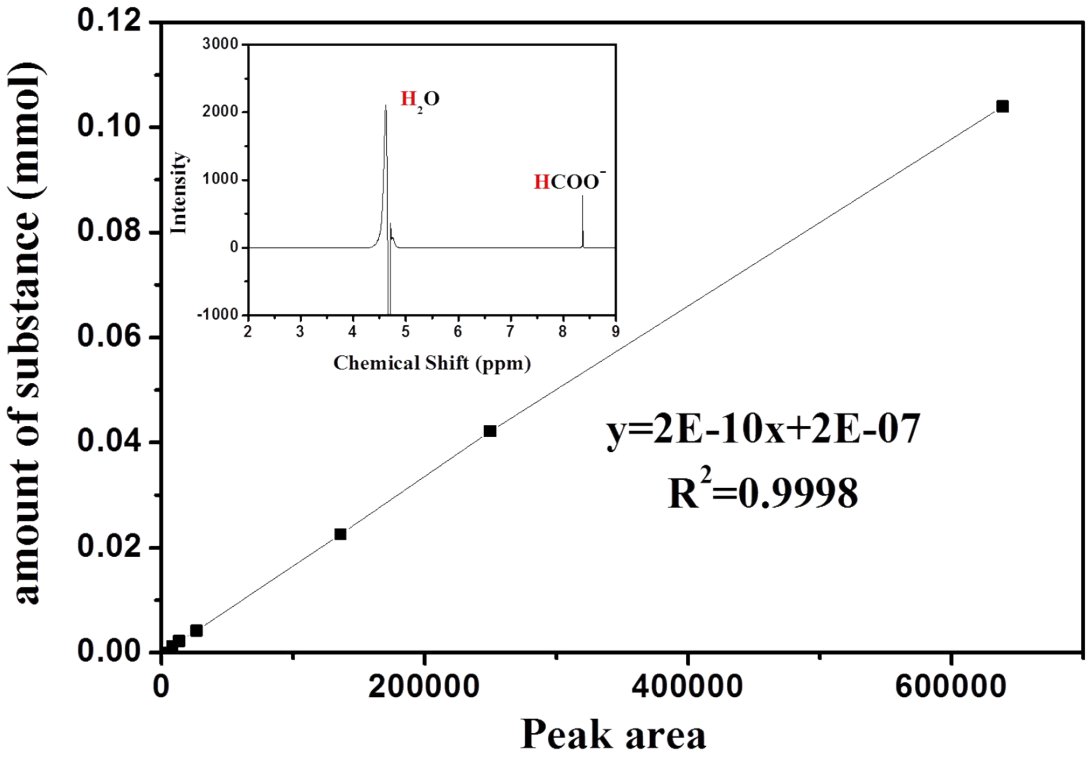


**Fig. S11** The relationship between the n(HCOOH) and peak area from NMR.

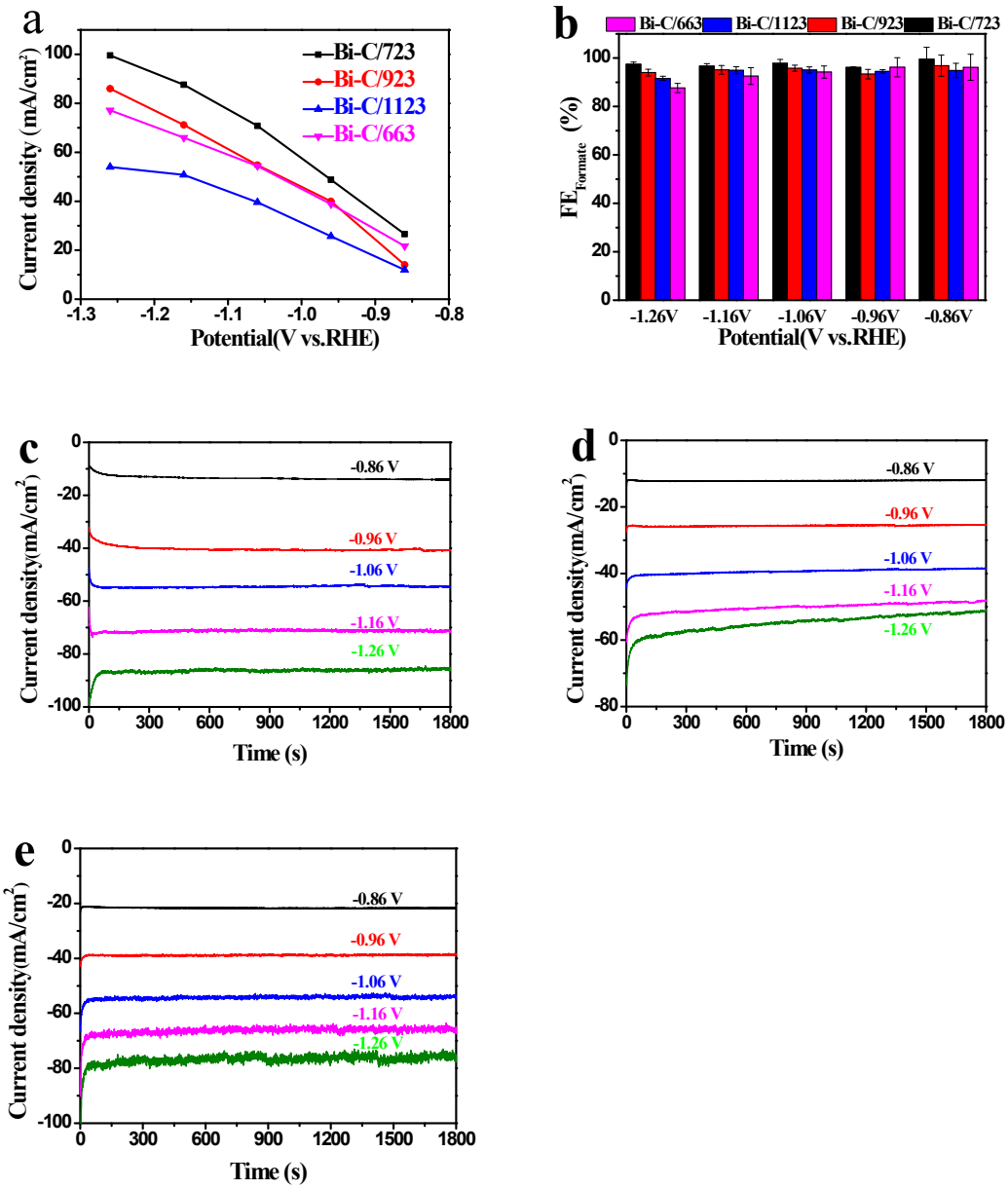


**Fig. S12** a) Current densities and b) FEformate at different potential for electrochemical reduction of $CO_2$ of Bi-C materials in $CO_2$-saturated 0.5 M $KHCO_3$. c) The amperometric i-t Curves for the detailed ECR process of Bi-C/923. d) The amperometric i-t Curves for the detailed ECR process of Bi-C/1123. e) The amperometric i-t Curves for the detailed ECR process of Bi-C/663.

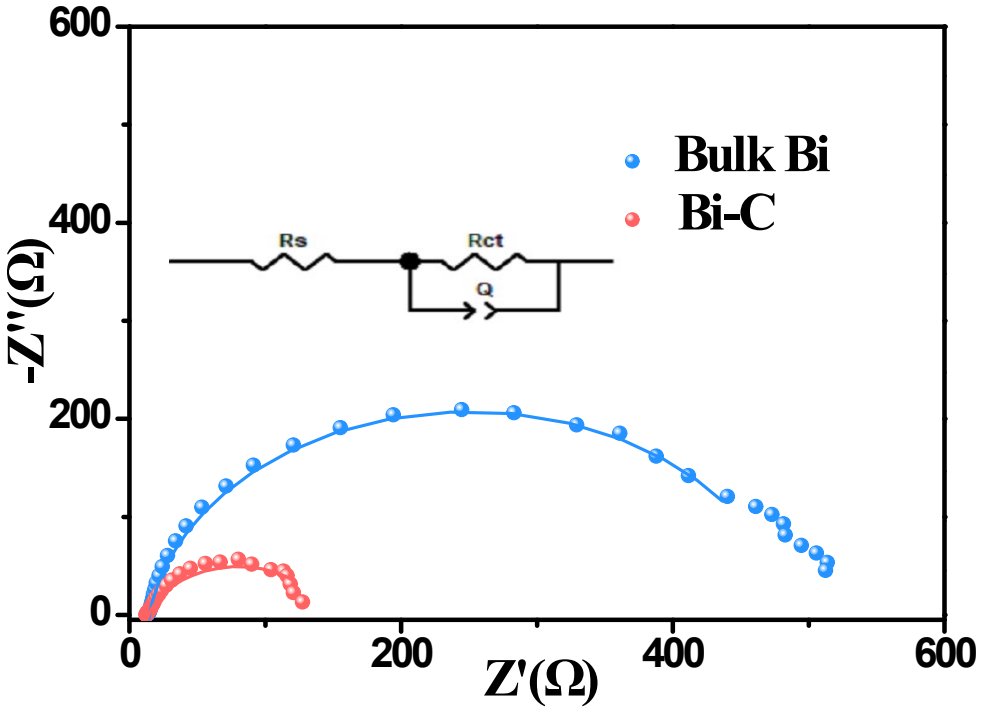


**Fig. S13** Nyquist plots for Bi-C/723 and bulk Bi at -0.76V vs. RHE.

The electrochemical impendence spectroscopy (EIS) was applied to analyze the charge transfer between the electrolyte and catalyst interface. The Nyquist plots are showed in Fig. 4d (the inset shows equivalent circuit diagram). Rs represents the resistance of electrolyte solution, while Rct is related to the resistance of charge exchange between the catalyst and reactants in the electrolyte which was directly proportional to the diameter of the semicircle in the spectra. Apparently, the diameter of the semicircle of Bi-C/723 is much smaller than that of the bulk Bi. The Nyquist plots were further fitted by Zview and the Rct of Bi-C/723 is 133 Ω which is much smaller than the Rct (471 Ω) of Bulk Bi.

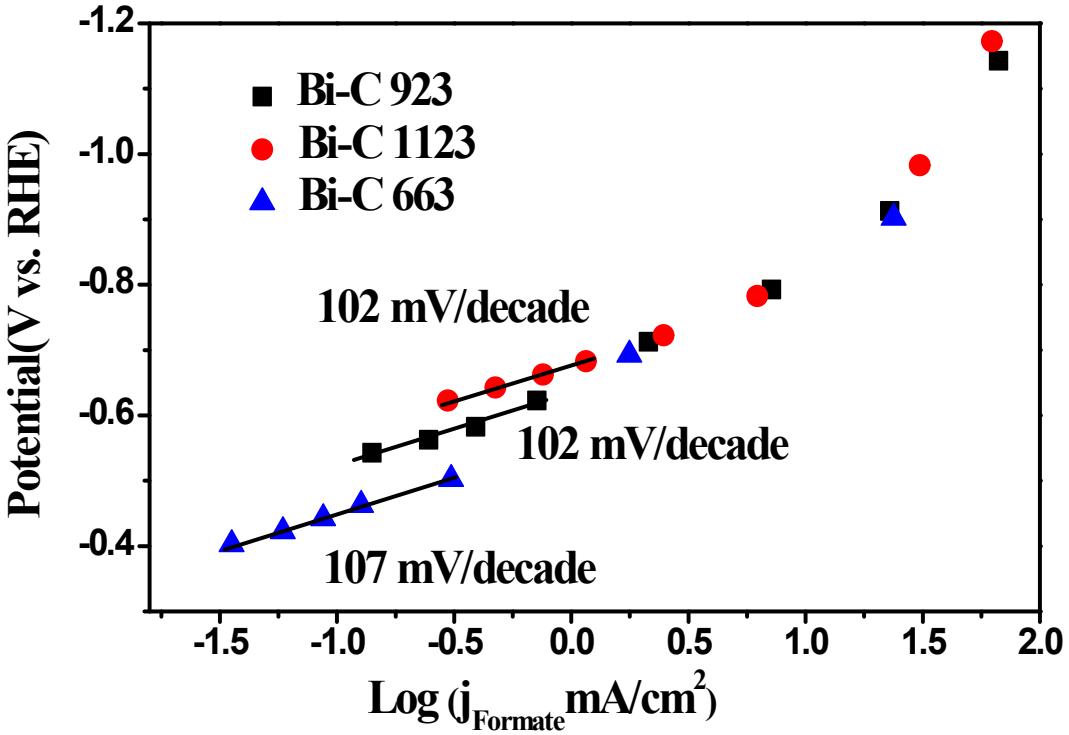


**Fig. S14** The tafel slope values of Bi-C/663 Bi-C/723 and Bi-C/1123.

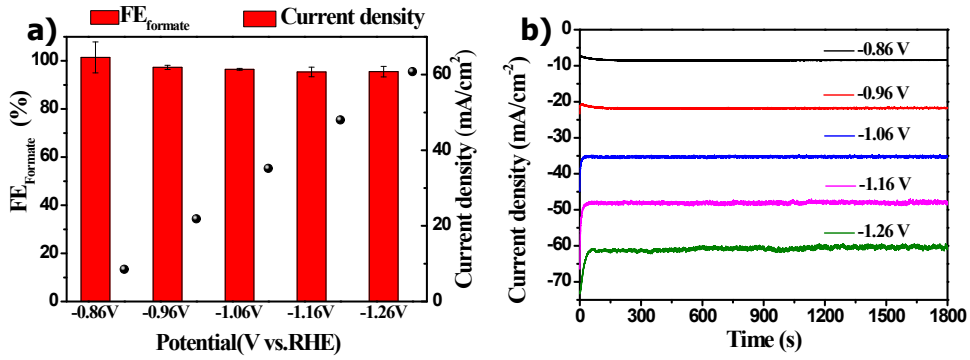


**Fig. S15 a)** Current densities and $FE_{formate}$ at different potential, b) the amperometric i-t Curves for electrochemical reduction of $CO_2$ of Bi-C/723K.

**Table S1.** The comparative study of current density and $FE_{formate}$ for recent Bi-based catalysts

| | Bi nanoflakes[1] | | Bismuth nanowires[7] | | Ultrathin Bi nanosheets[8] | | 2D Mesoporous Bi Nanosheets[9] | | Bismuthene[10] | | Superhydrophobic Bi-C (this work) | |
|---|---|---|---|---|---|---|---|---|---|---|---|---|
| Eletrolyte | 0.1 M $KHCO_3$ | | 0.5 M $NaHCO_3$ | | 0.5 M $NaHCO_3$ | | 0.5 M $NaHCO_3$ | | 0.5 M $KHCO_3$ | | 0.5 M $KHCO_3$ | |
| substrate | Cu metal film | | Cu foam | | carbon fiber paper | | carbon fiber paper | | carbon paper | | carbon paper | |
| Potential (V vs. RHE) | **Current density ($mA\ cm^{-2}$)** | **$FE_{formate}$ (%)** | **Current density ($mA\ cm^{-2}$)** | **$FE_{formate}$ (%)** | **Current density ($mA\ cm^{-2}$)** | **$FE_{formate}$ (%)** | **Current density ($mA\ cm^{-2}$)** | **$FE_{formate}$ (%)** | **Current density ($mA\ cm^{-2}$)** | **$FE_{formate}$ (%)** | **Current density ($mA\ cm^{-2}$)** | **$FE_{formate}$ (%)** |
| -0.86 | 3.1 | 101 | 25 | 93 | 13 | 90 | 10 | 95 | 9 | 93 | 27 | 99 |
| -0.96 | 3.1 | 103 | 37 | 94 | 16 | 94 | 15 | 98 | 10 | 88 | 49 | 96 |
| -1.06 | 3.2 | 59 | 45 | 95 | 22 | 95 | 16 | 87 | 14 | 80 | 70 | 97 |
| -1.16 | 2 | 52 | 47 | 87 | 24 | 79 | 17 | 86 | 20 | 70 | 88 | 96 |
| -1.26 | 2.5 | 30 | 46 | 82 | | | | | | | 100 | 97 |

**References**


1. S. Kim, W. J. Dong, S. Gim, W. Sohn, J. Y. Park, C. J. Yoo, H. W. Jang and J.-L. Lee, *Nano Energy*, 2017, **39**, 44-52.
2. E. Zhang, T. Wang, K. Yu, J. Liu, W. Chen, A. Li, H. Rong, R. Lin, S. Ji, X. Zheng, Y. Wang, L. Zheng, C. Chen, D. Wang, J. Zhang and Y. Li, *J. Am. Chem. Soc.*, 2019, **141**, 16569-16573.
3. Y. Liu, G. Wang, J. Dong, Y. An, B. Huang, X. Qin, X. Zhang and Y. Dai, *J. Colloid Interface Sci.*, 2016, **469**, 231-236.
4. H. R. Jeon, D. W. Lee and K. M. Ok, *J. Solid State Chem.*, 2012, **187**, 83-88.
5. N. Tsumori, L. Chen, Q. Wang, Q.-L. Zhu, M. Kitta and Q. Xu, *Chem.*, 2018, **4**, 845-856.
6. P. Deng, H. Wang, R. Qi, J. Zhu, S. Chen, F. Yang, L. Zhou, K. Qi, H. Liu and B. Y. Xia, *ACS Catal.*, 2019, **10**, 743-750.
7. X. Zhang, X. Sun, S.-X. Guo, A. M. Bond and J. Zhang, *Energy Environ. Sci.*, 2019, **12**, 1334-1340.
8. N. Han, Y. Wang, H. Yang, J. Deng, J. Wu, Y. Li and Y. Li, *Nat. Commun.*, 2018, **9**, 1320.
9. H. Yang, N. Han, J. Deng, J. Wu, Y. Wang, Y. Hu, P. Ding, Y. Li, Y. Li and J. Lu, *Adv. Energy Mater.*, 2018, **8**, 1801536.
10. F. Yang, A. O. Elnabawy, R. Schimmenti, P. Song, J. Wang, Z. Peng, S. Yao, R. Deng, S. Song, Y. Lin, M. Mavrikakis and W. Xu, *Nat. Commun.*, 2020, **11**, 1088.